ACS APPLIED MATERIALS & INTERFACES

RESEARCH ARTICLE

www.acsami.org

Electrical and Optical Properties of Diketopyrrolopyrrole-Based Copolymer Interfaces in Thin Film Devices

Danish Adil,[†] Catherine Kanimozhi,[‡] Ndubuisi Ukah,[†] Keshab Paudel,[†] Satish Patil,*[,‡] and Suchi Guha*[,†]

[†]Department of Physics and Astronomy, University of Missouri, Columbia, Missouri 65211, United States

[‡]Solid State and Structural Chemistry Unit, Indian Institute of Science, Bangalore, India, 560012

ABSTRACT: Two donor−acceptor diketopyrrolopyrrole (DPP)-based copolymers (PDPP-BBT and TDPP-BBT) have been synthesized for their application in organic devices such as metal−insulator semiconductor (MIS) diodes and field-effect transistors (FETs). The semiconductor-dielectric interface was characterized by capacitance−voltage and conductance−voltage methods. These measurements yield an interface trap density of 4.2×10^{12} $eV^{-1}cm^{-2}$ in TDPP-BBT and 3.5×10^{12} $eV^{-1}cm^{-2}$ in PDPP-BBT at the flat-band voltage. The FETs based on these spincoated DPP copolymers display p-channel behavior with hole mobilities of the order 10^{-3} $cm^2/(V\ s)$. Light scattering studies from PDPP-BBT FETs show almost no change in the Raman spectrum after the devices are allowed to operate at a gate voltage, indicating that the FETs suffer minimal damage due to the metal−polymer contact or the application of an electric field. As a comparison Raman intensity profile from the channel-Au contact layer in pentacene FETs are presented, which show a distinct change before and after biasing.

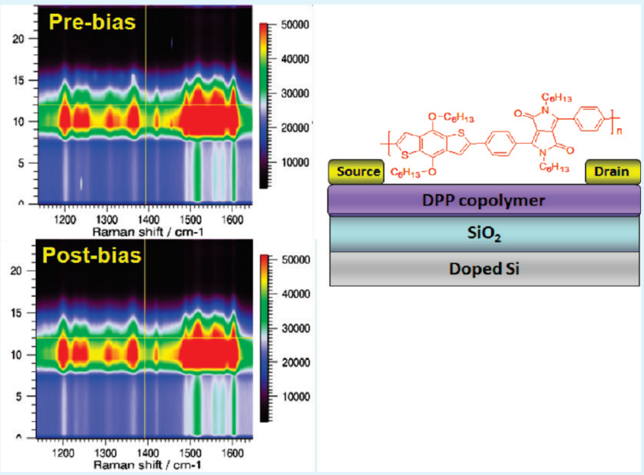

KEYWORDS: diketopyrrolopyrrole, donor−acceptor, metal−insulator−semiconductor, field-effect transistors, capacitance−voltage characteristics, Raman scattering

1. INTRODUCTION

The design of systems incorporating both donor and acceptor chromophores are of particular interest for applications in bipolar field-effect transistors and solar cells. Oligomers and polymers based on donor−acceptor moieties have a high degree of tunability of their electronic and optical properties as the relative contribution of the electron-rich and −poor components may be controlled. Diketopyrrolopyrrole (DPP) containing copolymers have recently gained a lot of interest in organic optoelectronics.[1−6] Near-infrared light-emitting polymer field-effect transistors (FET) have been demonstrated using DPP-based copolymers.[7] Recently, DPP-based polymers have been synthesized which show ambipolar transport in FETs with nearly balanced electron and hole mobilities.[8,9] Organic photovoltaics based on DPP polymers and oligomers show overall power conversion efficiencies (PCE) of 4.4%.[10] Introducing electron-rich and electron-deficient alternating units in a polymer chain allow tuning of its highest occupied molecular orbital (HOMO) level with respect to the lowest unoccupied molecular orbital (LUMO) level of the acceptor molecule, which helps to increase the open circuit voltage in solar cells. Several other donor−acceptor (D-A) type copolymers have been used in solar cells to achieve PCE of above 5% with extensive device engineering efforts.[11−13]

DPP has been extensively used as high performance industrial pigment owing to its extraordinary thermo- and photostability and high optical density. The intermolecular hydrogen bonding in nonalkylated DPP core forms a two-dimensional network combined with $\pi-\pi$ and van der Waals interactions between molecular planes, and leads to films that self-assemble into ordered domains. This makes them highly desirable for FET applications as the field-effect mobilities are enhanced. Small organic molecules/oligomers in FETs show higher charge carrier mobilities compared to long-chain polymers. A majority of these organic molecules are hole conductors; among them pentacene,[14] rubrene,[15] and oligothiophene derivatives[16,17] show some of the highest room temperature carrier mobilities. Supramolecular organization of polymeric semiconductors in thin films typically enhances FET performance. DPP-based low bandgap materials are not just useful for device applications but are desired to achieve environmentally stable organic semiconductors. The strong intermolecular interaction leads to molecular packing with a large electronic bandwidth, thus improving the charge-transport properties.

This work reports the application of two DPP-based copolymers in organic FETs and metal−insulator-semiconductor (MIS) diode: poly{2,6′-4,8-dihexyloxybenzo[1,2-*b*;3,4-*b*]dithiophene-alt-2,5-dihexyl-3,6-bis-(4-phenyl-1-yl)pyrrolo[3,4-*c*]pyrrole-1,

Received: January 9, 2011
Accepted: March 31, 2011
Published: March 31, 2011

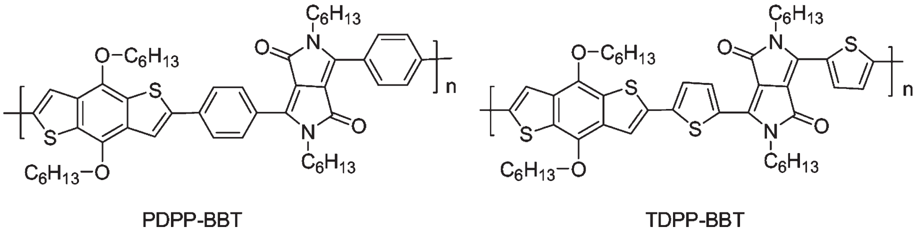

Figure 1. Chemical structures of PDPP-BBT and TDPP-BBT.

Scheme 1. Synthesis of the Copolymers TDPP-BBT and PDPP-BBT by Stille Coupling

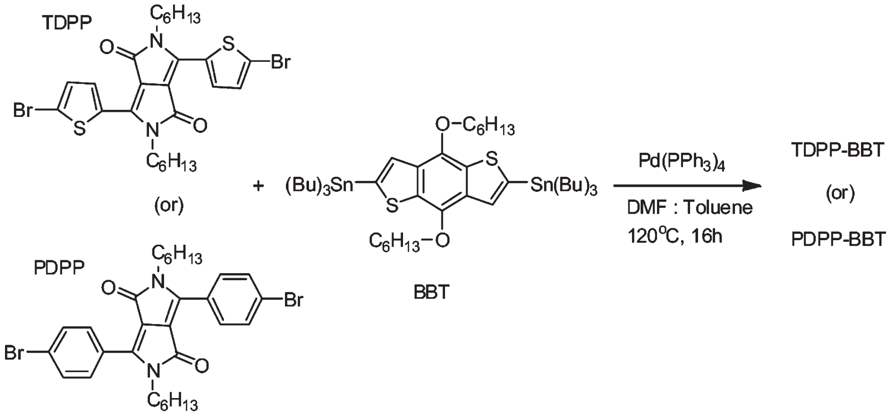

4-dione}(PDPP-BBT) and poly{2,6′-4,8-dihexyloxybenzo[1,2-*b*; 3,4-*b*]dithiophene-alt-2,5-dihexyl-3,6-bis(5-thiophen-2-yl)pyrrolo[3,4-*c*]pyrrole-1,4-dione} (TDPP-BBT) (Figure 1). Recently it has been demonstrated that these DPP copolymers yield almost a 3% PCE when utilized in unoptimized organic solar cells.[18] The optical properties of the two copolymers were discussed in detail in ref 18. The absorption spectra show peaks at 563 and 656 nm for PDPP-BBT and TDPP-BBT films, respectively. The FET characteristics of the DPP copolymers correlate with the morphology of the films and capacitance−voltage characteristics of their corresponding MIS diode structures. Both copolymers exhibit p-type FET characteristics with hole mobilities in the range $10^{-3}-10^{-4}$ cm^2/(V s) for spincoated films and depends upon the molecular weight. Raman spectroscopy was used to generate maps of the vibrational spectra from the active device region of PDPP-BBT FETs before and after biasing the devices. No degradation of the polymer film, either structural or because of charge injection and transport, was observed. For a comparison, we also highlight the Raman maps from similar pentacene-based FETs, where changes are seen before and after biasing the devices; some of the changes in the Raman spectra are attributed to structural changes of the molecule.

2. EXPERIMENTAL SECTION

2. 1. Materials.

Tetrakis(triphenylphosphine)palladium(0) (Pd(PPh$_3$)$_4$), 1-hexyl bromide, 3-bromo thiophene, thiophene 3-carboxylic acid were obtained from Aldrich and used without further purification. *N*-Bromosuccinimide (NBS) was crystallized from hot water prior to use. THF, CHCl$_3$, and NMP were dried by Na/benzophenone, P$_2$O$_5$, and calcium hydride, respectively. Dry toluene and dry dimethyl formamide were purchased and used without further drying.

2.1.1. Synthesis of Polymers. The monomers **PDPP** (3,6-bis(4-bromophenyl)-2,5-dihexylpyrrolo[3,4-*c*]pyrrole-1,4-dione) and **TDPP** (3,6-bis(5-bromothiophen-2-yl)-2,5-dihexylpyrrolo[3,4-*c*]pyrrole-1,4-dione) were synthesized from previously reported procedures.[19−21] Both copolymers were synthesized from Stille coupling reaction. One mmol of PDPP or TDPP and 1 mmol of 2,6-bis(tributyltin)-4,8-dihexyloxybenzo[1,2-*b*;3,4-*b*]dithiophene were taken in a well dried two neck 100 mL round-bottom flask. A 1:4 ratio of dry dimethyl formamide and dry toluene was taken and this mixture was purged with argon for 15 min and refluxed at 120 °C. Under dark condition, catalytic amount of (Pd(PPh$_3$)$_4$) was added and the reaction mixture was evacuated and argon was passed for 3−4 times. This reaction mixture was refluxed at the same temperature for 16 h. Solvent was evaporated and the solid was dissolved in 3−4 mL of CHCl$_3$ and the crude solid was precipitated in MeOH. This solid was washed with MeOH, hexane, and acetone to remove low molecular weight compounds and solid was dried under vacuum. TDPP-BBT was obtained as a blue solid and PDPP-BBT was obtained as a brown solid. The molecular weight (M_w) of the polymers was determined by gel permeation chromatography using polystyrene standards in tetrahydrofuran and was found to be 9700 g/mol for PDPP-BBT and 3510 g/mol for TDPP-BBT (sample A). The FET characteristics were also performed for another sample of TDPP-BBT with a higher M_w (5080 g/mol) (sample B).

2.2. Fabrication of FETs and MIS Structures.

The devices were fabricated using a top-contact bottom gate structure with gold source and drain electrodes. Heavily p-doped silicon (100) wafers, with resistivity of 0.001−0.005 Ω-cm, were used as the gate electrode with 200 nm bare SiO$_2$ layer as the gate dielectric. The substrates were cleaved into ~1 in. × 1 in. pieces, ultrasonicated in acetone, rinsed with isopropyl alcohol, and finally submerged in Piranha solution (7:3 H$_2$SO$_4$/H$_2$O$_2$) at 115 °C for 15 min. OTS (Octadecyltrichlorosilane) from Sigma-Aldrich was used to form self-assembled monolayers on the SiO$_2$ surface by submerging the substrates in a 0.01 M solution of OTS in toluene.

All fabrication steps including spincoating and evaporation for FETs and MIS structures were carried out in a nitrogen glovebox with oxygen and water levels below 1 ppm. Solutions of TDPP-BBT and PDPP-BBT (5 mg/mL) in chloroform were prepared and left to sit overnight. Prior to spin-casting, the solutions were filtered through a 0.22 μm PTFE filter to ensure no traces of undissolved impurities remained. About 0.25 mL of each solution was spun-cast onto the substrates at 2000 rpm. The thickness of the films was measured and found to be ~30 nm. The polymer films were then annealed in an oven at 100 °C for 30 min and left to cool slowly at room temperature. Top contacts of 30 nm Au were deposited for the source (S)-drain (D) contacts via thermal evaporation at a base pressure of 10^{-6} mbar through a shadow mask. Typical S-D channel length and width for FETs ranged from 0.050 to 0.075 mm and 0.25–0.75 mm, respectively. Pentacene FETs were fabricated using both SiO_2 and PMMA (polymethyl methacrylate) as gate dielectrics. High purity pentacene was obtained from Sigma Aldrich and used without any further purification. Fabrication of the devices based on a SiO_2 gate dielectric was identical to that of the DPP-based devices except that the pentacene was thermally evaporated onto the substrate. For the PMMA based devices, ~ 1 in. × 1 in. glass pieces with an 80 nm layer of thermally evaporated aluminum served as both the substrate and the gate electrode. PMMA (M_w = 996 000 g/mol) dissolved in butyl acetate (8 wt %) was spun-cast at 2000 rpm. The PMMA film was then baked in an oven at 100 °C for 60 min. All subsequent fabrication steps were identical to that of the SiO_2 based devices. The device area for MIS structures was determined by a scanning electron microscopy to be $2.2 \pm 0.1 \times 10^{-3}$ cm^2.

2.3. Instrumental Analysis. The atomic force microscope (AFM) measurement was performed with a Nanoscope IIIa (Veeco Instruments, Inc.) operating in the tapping mode. Commercial ultrasharp, rectangular silicon cantilevers made by Micromasch ($250 \times 35 \times 1.7\ \mu m^3$) were used having a nominal spring constant of ~0.35 N/m and a resonance frequency of ~33 kHz.

The FET characteristics were measured at room temperature in a stream of dry nitrogen with two source meters, Keithley 2400 and Keithley 236, configured together using a program written in LabView. The source-drain current and the source-gate leakage currents were measured with Keithley 236, which has a resolution of 10 fA.

Conductance-frequency measurement in the 20 Hz to 1 MHz range, capacitance–voltage (C–V) and conductance-voltage (G-V) measurements in the frequency range of 500 to 800 Hz were carried out using an HP 4284A precision LCR meter. The devices were biased from −40 V to +10 V at a sweep rate of 80 mV/s for C–V and G-V measurements. Since no offsets were observed in the measured and calculated accumulation capacitances in the frequency range for our measurements, no corrections were made for the series resistance.

The Raman spectra of the PDPP-BBT films from FETs were collected by an Invia Renishaw spectrometer attached to a microscope with a × 50 lens. The samples were excited with a 785 nm diode laser (~5mW). Linescans consisting of about 25 individual measurements taken in the channel region of the FET and through the Au contact immediately adjacent to the channel region at 5 μm intervals were measured to generate 2-dimensional maps. These maps help visualize any structural or electronic changes to the polymer layer due to the interaction of the semiconductor with the Au contact. The Raman linescans were further measured after biasing the FET to an external gate voltage. Biasing the FET was accomplished by running the devices until there was at least a −5 V shift in the threshold voltage as determined from the transfer current–voltage curve. No Raman spectroscopy was measured on TDPP-BBT-based FETs since the material's absorbance overlapped the laser wavelength.

3. RESULTS

3.1. AFM Studies. Thin films for AFM studies were spincoated on cleaned Si substrates using similar conditions as in FETs and MIS structures. Both as-is and annealed films were used for this study. The annealed films for this study were thermally treated similar to those in the FET structures. The scans were carried out in a tapping mode. Figure 2 shows the AFM images of both as-is and annealed films of PDPP-BBT (a, b) and TDPP-BBT (c, d) for 2 μm × 2 μm area. The AFM images are shown only for sample A (TDPP-BBT). The images on the left are from as-is films and on the right are the annealed films. The root-mean-square (rms) value of the surface roughness of as-is and annealed PDPP-BBT films are 1.32 and 1.29 nm, respectively. The rms value of the surface roughness of as-is and annealed TDPP-BBT films are 4.4 and 3.8 nm, respectively. The higher rms roughness for TDPP-BBT films (sample A) may be related to its lower molecular weight compared to the PDPP-BBT copolymer.

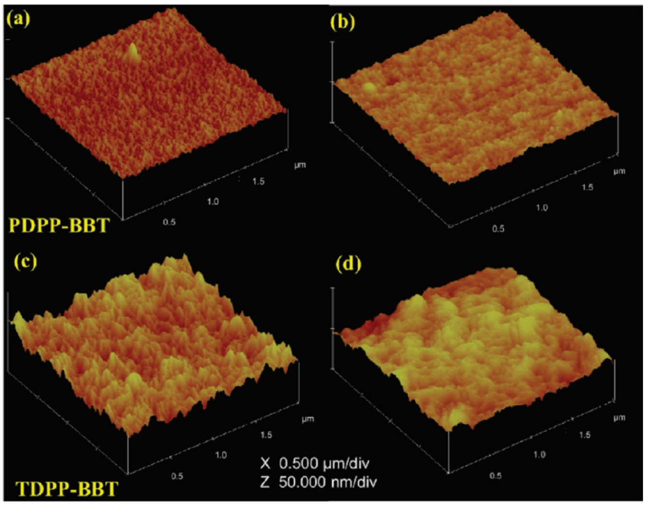

Figure 2. AFM images from films of (a) as-is PDPP-BBT, (b) annealed PDPP-BBT, (c) as-is TDPP-BBT, and (d) annealed TDPP-BBT.

3.2. Capacitance Measurements from MIS Structures. The quality of an interface between an insulator and a semiconducting polymer determines the performance of polymer FETs. In particular, trapped and interfacial charges have significant impact on the performance of organic light-emitting diodes (LEDs) and FETs resulting in voltage instability and delay time of electroluminescence at low operation voltages. Good interfaces between the polymer semiconductor and dielectrics are extremely crucial for practical device operation and application. Capacitance and conductance measurements allow the extraction of material parameters, such as doping density, mobility, and interface states density. All MIS and FET structures were fabricated with annealed films of the copolymers. The TDPP-BBT results are for sample A.

Figure 3 shows the C–V plots of p^+Si/SiO_2/PDPP-BBT/Au and p^+Si/SiO_2/TDPP-BBT/Au MIS diodes. The inset shows the hysteresis at 600 Hz frequency. The shift of the flat band voltage merely indicates a mismatch of the work function of the metal and the organic semiconductor. The C–V curves demonstrate the p-type nature of the copolymer: higher capacitance in the accumulation regime, corresponding to the insulator capacitance C_O (SiO_2) at negative bias, which decreases with increasing voltage consistent with the formation of a depletion region at the PDPP-BBT/SiO_2 and TDPP-BBT/SiO_2 interface, and lower capacitance in the depletion region at more positive bias. At voltages of −10 V and −15 V, the capacitance falls to ~33 pF and ~34 pF in PDPP-BBT and TDPP-BBT MIS structures, respectively. These capacitances reflect the series sums of C_O and bulk semiconductor capacitance, C_B. Thus, it could be deduced that an applied voltage greater than −10 V fully depletes the semiconducting layers. Hence, with C_B of ~285 pF in PDPP-BBT MIS and ~181 pF in TDPP-BBT MIS, we estimate film thicknesses of ~21 nm and

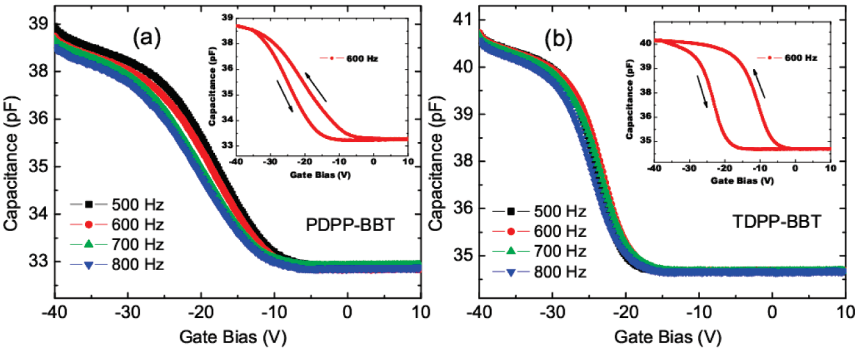

Figure 3. Capacitance vs voltage plots of (a) PDPP-BBT and (b) TDPP-BBT MIS diodes. The inset exhibits hysteresis curve for the same device at 600 Hz. The arrows indicate sweep direction of the gate bias voltage.

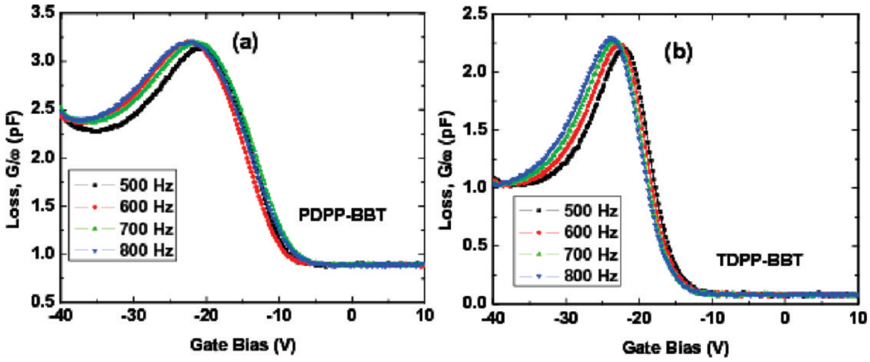

Figure 4. Loss (conductance/angular frequency) vs voltage plots of (a) PDPP-BBT and (b) TDPP-BBT MIS diodes obtained at four different frequencies.

~33 nm for the two structures, respectively assuming a dielectric constant of 3.0.[18]

We observe a hysteresis $\Delta = 2$ V and $\Delta = 10$ V (600 Hz) at the flat band voltages for PDPP-BBT and TDPP-BBT, respectively. Brown et al.[22] have attributed such a hysteresis to slow trapping (relaxation) of induced charge carriers or migration of low-mobility dopant ions toward the accumulation layer. Additionally, the hysteresis direction reveals the nature of charge injection. Counterclockwise loop of the hysteresis in the $C-V$ curve of organic MIS diode reveals a positive carrier injection into the organic layer with subsequent trapping.[23]

The frequency dispersion (FD) of the $C-V$ curves in the forward direction in the accumulation region most probably arises from different responses of trapped and mobile charges at the interface region. The FD can thus be directly related to the long relaxation time in the polymer.[24] The shallow states respond to voltages at high frequencies since the capture and emission of charges in these states have small time constants, while deep states with long time constants are localized, and thus do not respond to voltages at high frequency. The FD in the accumulation region of the PDPP-BBT sample within the given frequency range is slightly higher compared to the TDPP-BBT sample.

According to the Schottky−Mott analysis we can extract the doping density (or more pertinently the concentration of localized charges) from the relationship

$$\frac{\partial\left(\frac{1}{C^2}\right)}{\partial V} = \frac{2}{q\varepsilon_0\varepsilon_{\mathrm{semi}}N_{\mathrm{A}}A^2} \qquad (1)$$

where C is the capacitance in the depletion region, ε_{o} is permittivity of vacuum, $\varepsilon_{\mathrm{semi}}$ is the relative permittivity of the semiconductor, A is the device area, and N_{A} is the acceptor doping density. Assuming $\varepsilon_{\mathrm{semi}}$ as 3.0, N_{A} is estimated to be 4.4×10^{17} cm^{-3} at 600 Hz.

The presence of loss peaks (measured conductance per angular frequency) in Figure 4 indicates that energy loss in the devices is dominated by generation and recombination through interface trap levels.[25] The loss peaks increase slightly in magnitude and shift to lower voltages with increase in frequency, a characteristic feature of the distribution of the interface trap states in energy. The TDPP-BBT MIS shows a shift in the loss peak by 2.0 V compared to a 1.4 V shift in the PDPP-BBT MIS diode from 500 to 800 Hz. The use of the conduction technique[25] in the depletion region enables the extraction of the interface states density, capture probability and time constant dispersion of the majority carriers (holes in this case) from the real component of the admittance. These interface trap states change occupancy over a few $k_{\mathrm{B}}T/q$ wide centered about the Fermi level by interacting with the semiconductor bands via the emission and capture of carriers. A small ac signal applied to the gate of an MIS diode results in an alternate movement of the band edges toward or away from the Fermi level. Using the conductance technique, interface trap states are detected through the loss resulting from changes in their occupancy due to small variations in dc gate bias. This loss is shown as an ac conductance and by measuring the capacitance and conductance as a function of voltage and frequency, respectively (at a bias in depletion), the density of interface states may be obtained from the conductance loss due to these states.

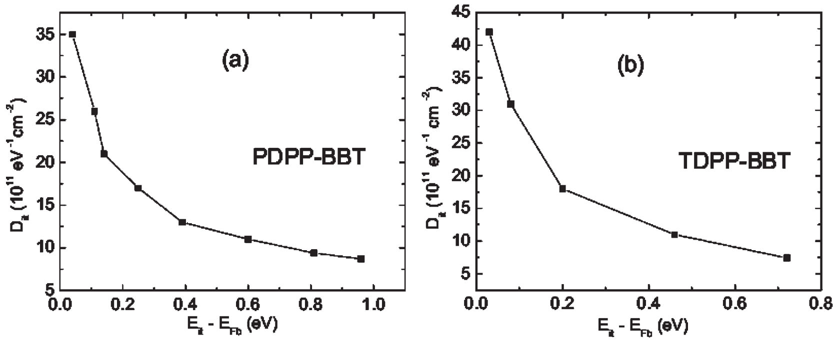

Figure 5. Density of interface traps (D_{it}) for (a) PDPP-BBT/SiO$_2$ and (b) TDPP-BBT/SiO$_2$ interfaces plotted as a function of energy above the bulk Fermi level, E_{Fb}.

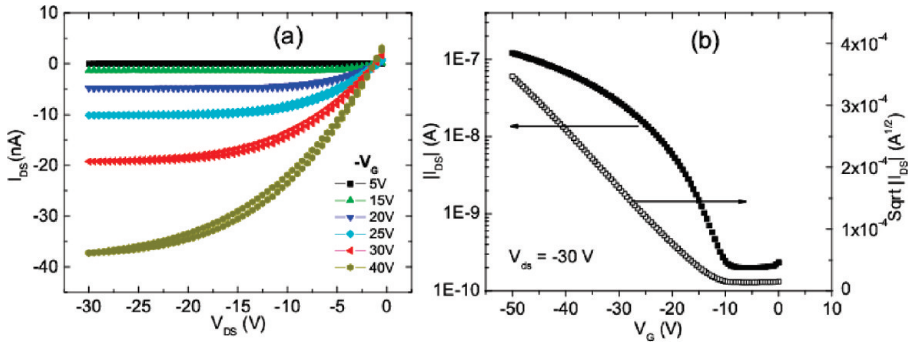

Figure 6. (a) Output and (b) transfer characteristics of PDPP-BBT FET.

A determination of the interface trap energy states, E_{it} is easily carried out by calculating the degree of band bending (in eV), $E_{it} - E_{Fb}$, induced by the applied voltage, via the solution of the Poisson equation in the depletion approximation

$$E_{it} - E_{Fb} = \frac{qN_A\varepsilon\varepsilon_0A^2}{2C_d{}^2} \qquad (2)$$

where E_{Fb} is the bulk semiconductor Fermi level and C_d is estimated at the relevant voltage considering that the measured capacitance is a series sum of C_O and C_B. With the interface states distributed in energy, we estimate the density of interface traps, D_{it}, using the relation[25]

$$\frac{G_p}{\omega} = C_{it}(2\omega\tau)^{-1}\ln[1 + (\omega\tau)^2] \qquad (3)$$

where $C_{it} = qD_{it}$ is the interface trap capacitance and τ is the interface state time constant. The maximum value of G/ω occurs at 1.98.

From Figure 5 it is observed that the interface trap density decreases from 3.5×10^{12} eV^{-1}cm^{-2} to 8.7×10^{11} eV^{-1} cm^{-2} over an energy range of 0.04–0.96 eV above the equilibrium Fermi level, and from 4.2×10^{12} eV^{-1}cm^{-2} to 7.4×10^{11} eV^{-1} cm^{-2} over an energy range of 0.03–0.72 eV, above the equilibrium Fermi level in PDPP-BBT and TDPP-BBT MIS diodes, respectively.

Overall the $C-V$ and $G-V$ plots of PDPP-BBT and TDPP-BBT MIS structures are comparable. The higher value of the measured loss (Figure 4) in the PDPP-BBT sample correlates to higher stretching of the $C-V$ curve in Figure 3. The slightly larger hysteresis in the C–V plot, higher shift of the loss peak, and a slightly higher D_{it} value close to the Fermi energy in TDPP-BBT MIS diode compared to PDPP-BBT MIS diode may be a result of the difference in the film morphology. However, the interface properties in terms of trap states between the polymer and the gate dielectric are comparable in the two MIS structures. The interface between the dielectric and the semiconductor may be significantly improved by using high-k polymer and hybrid dielectrics.[26]

3.3. Field-Effect Transistor Characteristics. The current–voltage characteristics of solution processed PDPP-BBT and TDPP-BBT (sample A) FETs on OTS treated Si/SiO$_2$ substrates are shown in Figures 6 and 7. Both the PDPP-BBT and the TDPP-BBT devices are p-type and show typical field-effect transistor behavior such as good modulation of drain-source current by gate voltage and drain-source current saturation at high gate voltages. There is almost no hysteresis in the output characteristics of the FETs as shown in Figure 6a. The leakage current was at least three-orders of magnitude smaller than the measured currents. The current–voltage characteristics of the TDPP-BBT FETs shown here have a W/L ratio of 10 and the PDPP-BBT devices shown here have a W/L ratio of 20. The FET characteristics were also measured from the higher M_w TDPP-BBT sample as shown in Figure 8. The FET characteristics were measured from at least 20 devices with different W/L ratios; almost all devices show similar characteristics.

Device parameters such as charge carrier mobility (μ), on/off current ratio, threshold voltage (V_{Th}) were estimated using the standard saturation regime current–voltage characteristics of field-effect transistors[27] with the drain-source current (I_{DS}) given by

$$I_{DS} = \frac{\mu WC_O}{2L}(V_G - V_{Th})^2 \qquad (4)$$

where C_O is the oxide capacitance, W and L are the channel width and length, respectively. V_G and V_{Th} are the gate voltage and

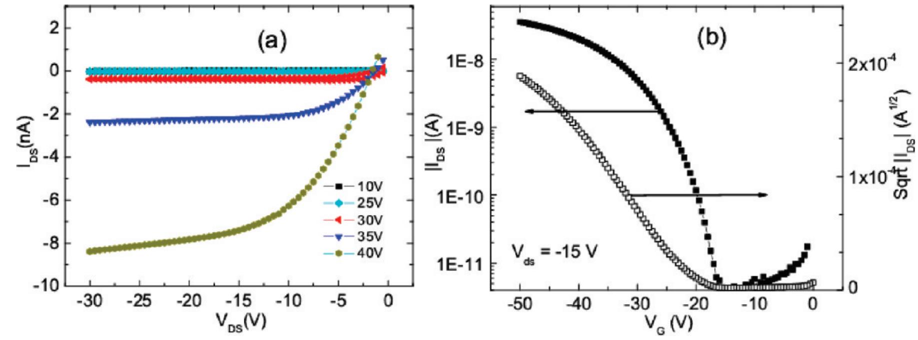

Figure 7. (a) Output and (b) transfer characteristics of TDPP-BBT (sample A) FET.

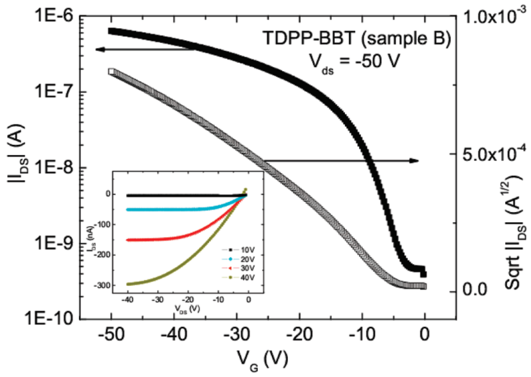

Figure 8. Transfer characteristics of TDPP-BBT (sample B) FET. The inset shows the output characteristics from the same device.

threshold voltages, respectively. Assuming the carrier mobility to be gate-voltage independent, eq 4 may be rearranged to give

$$\mu = \frac{2L}{WC_O}\left(\frac{\partial\sqrt{I_{DS}}}{\partial V_G}\right)^2 \tag{5}$$

The square root of the drain-source current as a function of the gate voltage is plotted in Figures 6b and 7b. A linear fit was applied to the saturation region to obtain the slope and from eq 5 the hole mobilities were found to be 1×10^{-3} $cm^2/(V\ s)$ for PDPP-BBT and 3×10^{-4} $cm^2/(V\ s)$ for TDPP-BBT (sample A). The on/off ratios for both FETs were ~10^3 for all samples. Sample B shows a considerably higher mobility of 7×10^{-3} $cm^2/(V\ s)$ as determined from the transfer characteristics of Figure 8.

Threshold voltages were determined by extrapolating the linear fit to zero drain-source current.[28] PDPP-BBT was found to have a threshold voltage of −11 V, TDPP-BBT (sample A) has a threshold voltage of −15 V, and TDPP-BBT (sample B) was found to have a threshold voltage of −5 V. The deviation of threshold voltages from being zero indicates that mobile holes accumulate in the PDPP-BBT/SiO_2 interface at a lower (in magnitude) gate voltage than they do at the TDPP-BBT/SiO_2 (sample B) interface. This result is consistent with the MIS characteristics, which show a slightly higher density of interface traps and the accumulation region occurring at a higher (in magnitude) gate voltage in TDPP-BBT.

The lower mobility in TDPP-BBT (sample A) cannot be attributed to the interface traps since the corresponding MIS structures reveal very similar interface properties for both TDPP-BBT and PDPP-BBT. We attribute the lower mobility in TDPP-BBT (sample A) to the actual film morphology due to its lower molecular weight compared to PDPP-BBT. This is also reflected in the AFM images which show a higher rms roughening in the TDPP-BBT films. In semicrystalline polymers, the molecular weight plays an important role in the actual packing of the polymer chains. In regioregular poly(3-hexylthiophene), the FET charge carrier mobilities increase by more than 3 orders of magnitude when the molecular weight increases by 3 orders of magnitude.[29] Our results point to the same trend. When the molecular weight of TDPP-BBT is increased by a factor of ~2, the charge carrier mobility is found to increase by an order of magnitude, as seen in Figure 8. Correlating the FET charge carrier mobilities in these DPP-based copolymers to their molecular weights is being currently pursued. Moreover, improving the polymer-dielectric interface by utilizing high-k dielectrics along with improved surface modification may result in improved FET characteristics with such DPP-based copolymers.

3.4. Raman Scattering Results. Raman spectroscopy is an extremely powerful, noninvasive tool for characterizing the physical and chemical properties of materials. For organic semiconductors, this technique is particularly informative on chemical composition, segmental orientation, conformational distribution and phase identification.[30] Most of these applications emphasize vibrational phonon spectroscopy. Recently, we have used Raman scattering to probe electron−phonon interaction in the presence of injected and photogenerated charge carriers in polyfluorene-based light-emitting diodes.[31] In here, we present Raman maps taken across the channel and the source/drain region of the FETs, both before and after biasing the FETs.

Intensity profiles of Raman linescans of PDPP-BBT and pentacene films from FET structures are shown in Figures 9 and 10, respectively. The pentacene data shown here are from FETs with PMMA as the dielectric layer. SiO_2-based pentacene FETs show similar results. Individual Raman spectra of PDPP-BBT and pentacene are shown in Figures 9c and 10c, respectively. PDPP-BBT has a number of Raman modes in the 1100−1700 cm^{-1} region. A recent experimental and theoretical work on pyridyl substituted DPP clarifies the origin of many of the peaks that we observe.[32] The 1600 cm^{-1} Raman peak is from the intraring C−C stretch motion (ring breathing) of the phenyl group. This is observed in all phenyl-based conjugated system.[33] The 1550 and 1364 cm^{-1} peaks originate from the C=C and C−C stretch of the central butadiene moiety, respectively.[32] The 1200 cm^{-1} Raman frequency is from a C−H bending motion of the phenyl ring,[34] which is not observed in TDPP-BBT.

A good description of pentacene Raman peaks is found in ref 35. The Raman peaks in the 1140−1190 cm^{-1} range originate from the C−H in-plane bending motion, and the C−C aromatic stretching vibration lies in the 1340−1400 cm^{-1} range. Figures 9a and 10a show the intensity distribution of the 1200 and 1363 cm^{-1} Raman peaks of

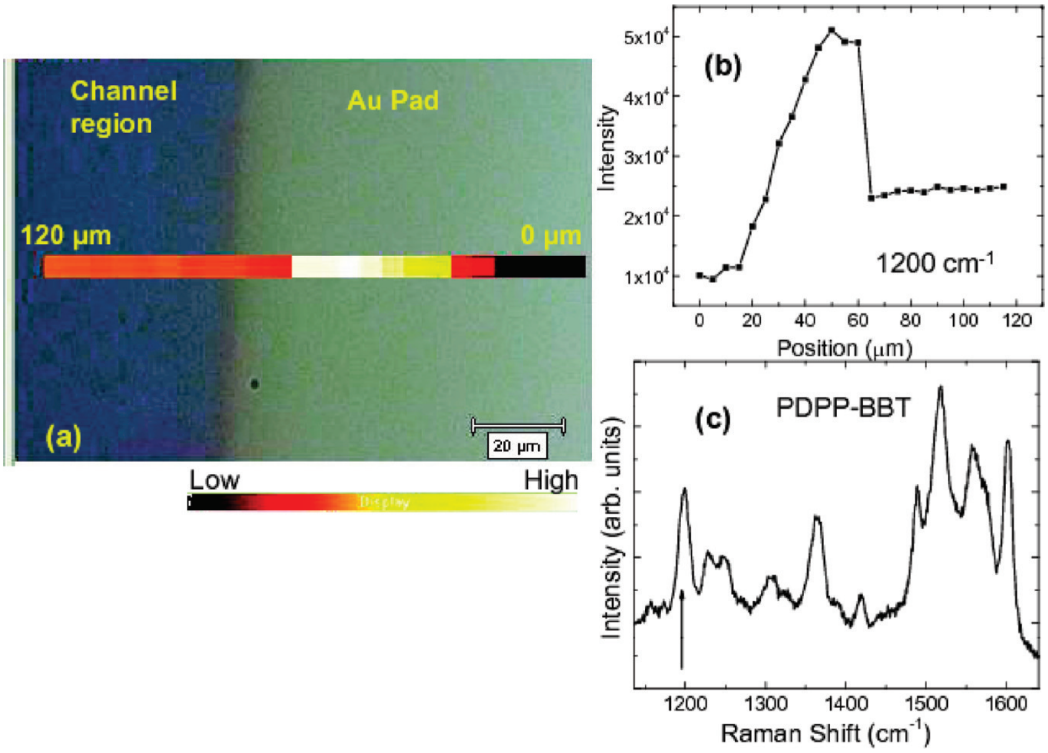

Figure 9. (a) Optical image of the channel/contact region in PDPP-BBT FET. (b) Intensity profile of the 1200 cm^{-1} Raman peak, corresponding to the color image in a. (c) Raman spectrum of PDPP-BBT.

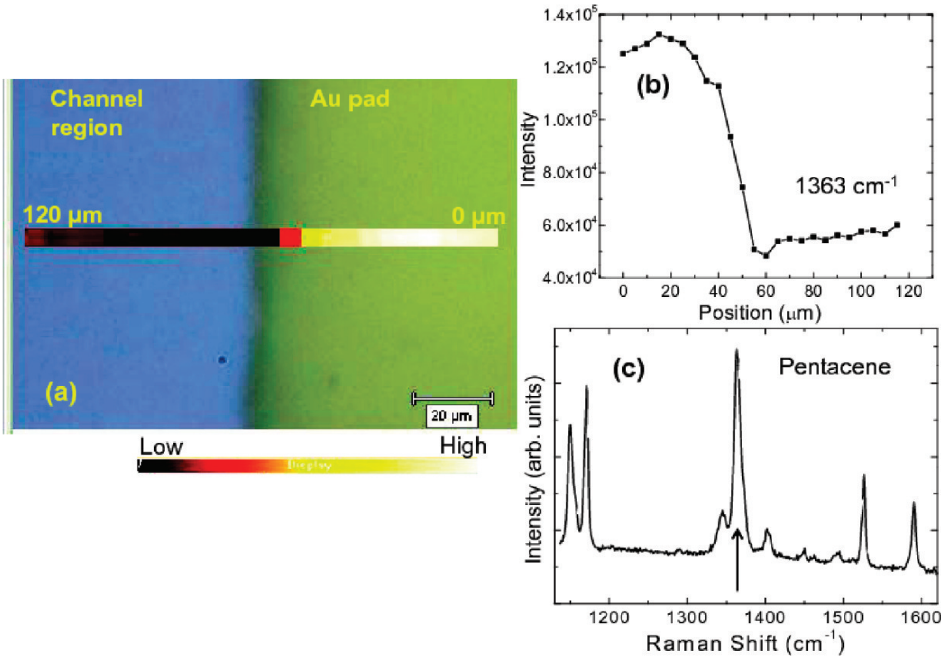

Figure 10. (a) Optical image of the channel/contact region in pentacene FET. (b) Intensity profile of the 1363 cm^{-1} Raman peak, corresponding to the color image in (a). (c) Raman spectrum of pentacene.

PDPP-BBT and pentacene films, respectively. The intensity profile of these peaks within the channel and the contact region (Figures 9b and 10b) is roughly indicative of the intensity of the remaining peaks in each spectrum. Each linescan map consists of ~24 spectra spanning 120 μm; the first measurement (0 μm) is taken over the Au contact and the last measurement is taken in the channel itself.

Along with changes in intensity of the Raman peaks of the semiconductor layer seen across the channel/Au pad region, enhancement of the Raman peaks from the dielectric layer (PMMA or SiO_2) is observed from the Au pad region in pentacene-based FETs (not shown here). This is most likely due to a surface-enhanced Raman scattering (SERS) effect, which

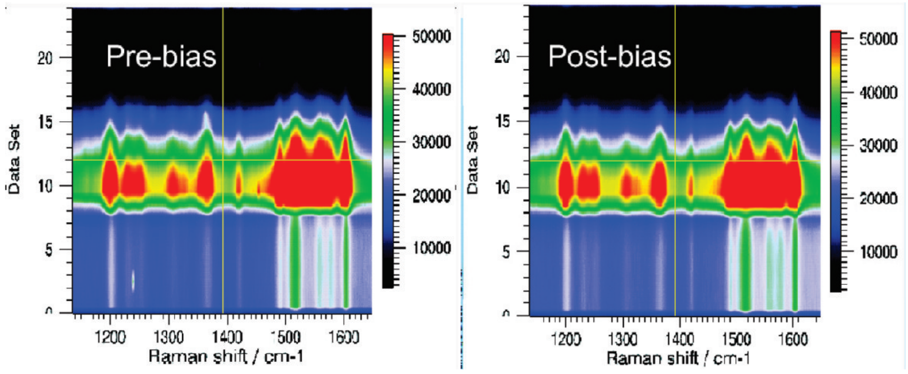

Figure 11. Raman maps of PDPP-BBT along the channel/contact region before and after biasing the FET.

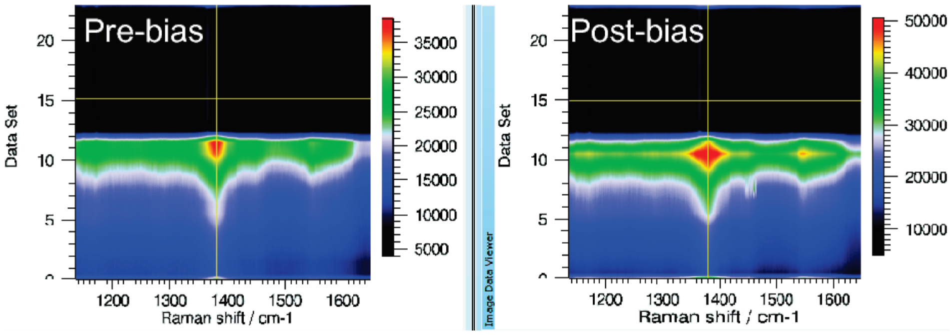

Figure 12. Raman maps of pentacene along the channel/contact region before and after biasing the FET.

is being currently investigated in more detail. Although the film thickness of the PDPP-BBT and pentacene are similar, no SERS effect from the underneath dielectric layer is observed in any of the PDPP-BBT FETs, which most likely is due to a difference in the nature of the initial Au monolayer on the polymer film.

Figure 11 shows the intensity profile of the Raman spectra in the 1150−1600 cm^{-1} range before and after biasing a PDPP-BBT FET. Data sets 0 and 24 correspond to 0 and 120 μm positions, respectively. Intensity enhancement of the Raman peaks is seen close to the edge of the Au contact and the channel region. There is almost no change observed in the Raman maps before and after biasing, indicating no induced structural changes in the polymer layer upon the application of the electric field. Raman measurements were performed on more than 10 devices, and they all showed a similar behavior. Furthermore, repeated electrical measurements in ambient conditions (under N_2 flow) over a few weeks showed no degradation in device performance.

We compare the Raman maps of PDPP-BBT with pentacene FETs (Figure 12), which were also measured before and after biasing. There is broadening of the Raman peak in the 1360 cm^{-1} region because of the SERS signal from PMMA; this is seen when the sample is probed over the Au contact. However, this effect is similar for pre- and postbiased devices. Comparing the two Raman maps in Figure 12, one clearly sees changes in the intensity profiles. These changes are irreversible. A careful analysis of the Raman spectrum before and after biasing the pentacene FETs show a reduction or a disappearance of the 1160 cm^{-1} peak. This has been observed in other works, where changes in the 1160 cm^{-1} region have been attributed to a structural phase transition induced by the source-to-drain electric field.[35] This is mainly due to a change in the herringbone packing of the pentacene molecule due to the source-drain electric field.[35] Our studies show further changes in the 1360 cm^{-1} region due to the presence of Au. Unlike PDPP-BBT, pentacene FETs show a reduction in mobilities after a few weeks when the devices have been operated many times. We are in the process of correlating the electrical characteristics of these FETs to the changes in the Raman maps. We also observe changes in the Raman maps of polyfluorene-based FETs, before and after biasing.

Intensity profile of the Raman spectra across the channel-contact region as shown in Figures 10 and 11 give a snapshot of the structural or electronic changes in the semiconductor layer due to the application of an external electric field. From the similarity of the Raman intensity profile before and after biasing in PDPP-BBT-based FETs, one may conclude that the devices suffer minimal or almost no damage due to the metal−polymer contact or the application of the electric field.

4. SUMMARY AND PROSPECT

In summary, diketopyrrolopyrrole-based copolymers, PDPP-BBT and TDPP-BBT, containing donor−acceptor structural units are promising candidates for solution processed p-channel FETs. Detailed capacitance−voltage studies were carried out from MIS structures based on the two copolymers. Interface trap density at the polymer/SiO_2 interface shows a similar behavior, whereby the D_{it} values decrease by almost an order of magnitude as one moves away from the Fermi energy. Close to the equilibrium Fermi level the D_{it} value (4.5×10^{12} eV^{-1}cm^{-2}) of TDPP-BBT MIS diode is slightly higher compared to PDPP-BBT MIS diode. The FET characteristics show a good modulation of drain-source current by gate voltage with almost no hysteresis in the current−voltage output characteristics. Charge carrier mobilities ~10^{-3} $cm^2/(V\ s)$ in spin-coated PDPP-BBT/TDPP-BBT FETs show that these DPP-based copolymers are excellent candidates for application in organic electronics.

The interface properties of PDPP-BBT FETs were further probed using Raman scattering. Raman linescans across the channel-contact region from devices before and after biasing show almost no changes indicating that there are no structural changes upon the application of an electric field. Furthermore, the metal−polymer contact seems to have no impact on the vibrational spectra, unlike pentacene or other fluorene-based devices. We have also shown some representative Raman maps from pentacene based FETs to illustrate that Raman maps from polymer-dielectric interfaces may be used to detect changes in the polymer structure upon the application of an electric field. Detailed microstructural studies aimed at correlating such polymer-dielectric interfaces with electrical properties of FETs are underway.

Studies on various processing conditions such as changing the solvent, utilizing different spin-on high-*k* dielectrics as a function of the polymer molecular weight of DPP-based polymers are currently under progress. It is conceivable that optimizing the polymer/dielectric interface may improve the FET charge carrier mobilities in such DPP-based copolymers by a few orders of magnitude.

AUTHOR INFORMATION

Corresponding Author

*E-mail: satish@sscu.iisc.ernet.in (S.P.); guhas@missouri.edu (S.G.). Tel: 1-573-884-3687 (S.G.). Fax: 1-573-882-4195 (S.G.).

ACKNOWLEDGMENT

We gratefully acknowledge the support of this work through the National Science Foundation under grant No. ECCS-0823563. S.P. thanks DST, India for funding under the fast track scheme for young scientists scheme through the project SR/FTP/CS-65/2006.

REFERENCES

(1) Zhang, K.; Tieke, B. *Macromolecules* **2008**, *41*, 7287.

(2) Zhu, Y.; Rabindranath, A. R.; Beyerlein, T.; Tieke, B. *Macromolecules* **2007**, *40*, 6981.

(3) Tantiwiwat, M.; Tamayo, A.; Luu, N.; Dang, X. D.; Nguyen, T. Q. *J. Phys. Chem. C.* **2008**, *112*, 17402.

(4) Huo, L.; Hou, J.; Chen, H. Y.; Zhang, S.; Jiang, Y.; Chen, T. L.; Yang, Y. *Macromolecules* **2009**, *42*, 6564.

(5) Zoombelt, A. P.; Mathijssen, S. G. J.; Turbiez, M. G. R.; Wienk, M. M.; Janssen, R. A. J. *J. Mater. Chem.* **2010**, *20*, 2240.

(6) Zhou, E.; Wei, Q.; Yamakawa, S.; Zhang, Y.; Tajima, K.; Yang, C.; Hashimoto, K. *Macromolecules* **2010**, *43*, 821.

(7) Bürgi, L.; Turbiez, M.; Pfeiffer, R.; Bienewald, F.; Kirner, H. J.; Winnewisser, C. *Adv. Mater.* **2008**, *20*, 2217.

(8) Bijleveld, J. C.; Zoombelt, A. P.; Mathijssen, S. J. G.; Wienk, M. M.; Turbiez, M.; de Leeuw, D. M.; Janssen, R. A. J. *J. Am. Chem. Soc.* **2009**, *1131*, 16616.

(9) Sonar, P.; Singh, S. P.; Li, Y.; Soh, M. S.; Dodabalapur, A. *Adv. Mater.* **2010**, *22*, 5409.

(10) Walker, B.; Tamayo, A. B.; Dang, X. D.; Zalar, P.; Seo, J. H.; Garcia, A.; Tantiwiwat, M.; Nguyen, T. Q. *Adv. Funct. Mater.* **2009**, *19*, 3063.

(11) Park, S. H.; Roy, A.; Beaupre, S.; Cho, S.; Coates, N.; Moon, J. S.; Moses, D.; Leclerc, M.; Lee, K.; Heeger, A. J. *Nat. Photonics* **2009**, *3*, 297.

(12) Hou, J. H.; Chen, J. Y.; Zhang, S. Q.; Li, G.; Yang, Y. *J. Am. Chem. Soc.* **2008**, *130*, 16144.

(13) Liang, Y. Y.; Wu, Y.; Feng, D. Q.; Tsai, S. T.; Son, H. J.; Li, G.; Yu, P. *J. Am. Chem. Soc.* **2009**, *131*, 56.

(14) Shibata, K.; Wada, H.; Ishikawa, K.; Takezoe, H. *Appl. Phys. Lett.* **2007**, *90*, 193509.

(15) Saeki, A.; Seki, S.; Takenobu, T.; Iwasa, Y.; Tagawa, S. *Adv. Mater.* **2008**, *20*, 920.

(16) Horowitz, G.; Hajlaoui, M. E. *Adv. Mater.* **2000**, *12*, 1046.

(17) Sun, Y.; Liu, Y.; Zhu, D. *J. Mater. Chem.* **2005**, *15*, 53.

(18) Kanimozhi, C.; Balraju, P.; Sharma, G. D.; Patil, S. *J. Phys. Chem. B.* **2010**, *114*, 3095.

(19) Tamayo, A. B.; Walker, B.; Nguyen, T. Q. *J. Phys. Chem. C.* **2008**, *112*, 11545.

(20) Rabindranath, A. R.; Zhu, Y.; Heim, I.; Tieke, B. *Macromolecules* **2006**, *39*, 8250.

(21) Hou, J.; Park, M. H.; Zhang, S.; Yao, Y.; Chen, L.; Li, J. H.; Yang, Y. *Macromolecules* **2008**, *41*, 6012.

(22) Brown, J.; Sirringhaus, H.; Harrison, M.; Shkunov, M.; Friend, R. H. *Phys. Rev. B.* **2001**, *63*, 125204.

(23) Yun, M.; Gangopadhyay, S.; Bai, M.; Taub, H.; Arif, M.; Guha, S. *Org. Electron.* **2007**, *8*, 591.

(24) Torres, I.; Taylor, D. M. *J. Appl. Phys.* **2005**, *98*, 073710.

(25) Nicollian, E. H.; Brews, J. R. *MOS Physics and Technology*; Wiley: New York; 2003.

(26) Oritz, R. P.; Facchetti, A.; Marks, T. J. *Chem. Rev.* **2010**, *110*, 205.

(27) Sze, S. M. *Semiconductor Devices-Physics and Technology*; Wiley: New York; 2002.

(28) Zaumseil, J.; Sirringhaus, H. *Chem. Rev.* **2007**, *107*, 1296.

(29) Kline, R. J.; McGehee, M. D.; Kadnikova, E. N.; Liu, J.; Fréchet, J. M. *J. Adv. Mater.* **2003**, *15*, 1519.

(30) Hsu, S. L. *Raman Scattering in Materials Science*; Weber, W. H., Merlin, R., Eds.; Springer-Verlag: Berlin, 2000; p 369.

(31) Arif, M.; Guha, S.; Tsami, A.; Scherf, U. *Appl. Phys. Lett.* **2007**, *90*, 252105.

(32) Lunak, S.; Vynuchal, J.; Horackova, P.; Frumarova, B.; Zak, Z.; Kuceri, J.; Salyk, O. *J. Mol. Struct.* **2010**, *39*, 983.

(33) Volz, C.; Arif, M.; Guha, S. *J. Chem. Phys.* **2007**, *126*, 064905.

(34) Guha, S.; Graupner, W.; Resel, R.; Chandrasekhar, M.; Chandrasekhar, H. R.; Glaser, R.; Leising, G. *Phys. Rev. Lett.* **1999**, *82*, 3625.

(35) Cheng, H. L.; Chou, W. Y.; Kuo, C. W.; Wang, Y. W.; Mai, Y. S.; Tang, F. C.; Chu, S. W. *Adv. Funct. Mater.* **2008**, *18*, 285.